

FlowBypass: Rectified Flow Trajectory Bypass for Training-Free Image Editing

Menglin Han¹ Zhangkai Ni¹

Abstract

Training-free image editing has attracted increasing attention for its efficiency and independence from training data. However, existing approaches predominantly rely on inversion–reconstruction trajectories, which impose an inherent trade-off: longer trajectories accumulate errors and compromise fidelity, while shorter ones fail to ensure sufficient alignment with the edit prompt. Previous attempts to address this issue typically employ backbone-specific feature manipulations, limiting general applicability. To address these challenges, we propose FlowBypass, a novel and analytical framework grounded in Rectified Flow that constructs a bypass directly connecting inversion and reconstruction trajectories, thereby mitigating error accumulation without relying on feature manipulations. We provide a formal derivation of two trajectories, from which we obtain an approximate bypass formulation and its numerical solution, enabling seamless trajectory transitions. Extensive experiments demonstrate that FlowBypass consistently outperforms state-of-the-art image editing methods, achieving stronger prompt alignment while preserving high-fidelity details in irrelevant regions.

1. Introduction

Image editing has become a powerful paradigm for controlling and manipulating visual content through intuitive instructions and prompts. Among various approaches, *training-free image editing* has gained increasing attention because it avoids the need for large-scale data or costly fine-tuning while still enabling flexible and effective manipulations. This property makes training-free methods especially appealing for practical deployment across diverse real-world applications.

However, a persistent challenge limits the effectiveness of

¹School of Computer Science and Technology, Tongji University, Shanghai, China. Correspondence to: Zhangkai Ni <zkni@tongji.edu.cn>.

existing training-free methods. Most existing approaches are built upon inversion–reconstruction trajectories, where an image is first inverted into noise and then reconstructed under the guidance of an edit prompt. This design inherently creates a trade-off: long trajectories accumulate estimation errors that erode **fidelity** in regions that should remain untouched, while short trajectories weaken **alignment** with the prompt, resulting in incomplete edits. Prior efforts to alleviate this trade-off include trajectory adjustments (Brack et al., 2024; Rout et al., 2025), prompt refinements (Mokady et al., 2023; Miyake et al., 2025), and feature manipulations (Hertz et al., 2023; Simsar et al., 2025). However, most of these methods traverse full trajectories, which exacerbates error accumulation near the inverted noise, and some rely on backbone-specific feature interventions, which hinder generality across generative models.

To overcome these limitations, we introduce **FlowBypass**, a general and analytical training-free image editing framework grounded in Rectified Flow (RF) (Liu et al., 2022). The central idea is a **trajectory bypass** that directly connects the inversion and reconstruction trajectories at intermediate states, thereby reducing accumulated estimation errors without relying on feature manipulations. This design not only addresses fidelity–alignment trade-offs but also ensures strong generalizability across diverse backbones. We develop FlowBypass starting from theoretical insights: we first analyze the inversion and reconstruction trajectories, then derive an approximate formulation of the bypass, and finally design a numerical solution via Euler discretization. This theoretical-to-practical pipeline enables efficient trajectory transitions while providing a unified solution applicable to a wide class of Rectified Flow models. Extensive experiments across diverse editing tasks demonstrate that FlowBypass consistently outperforms state-of-the-art training-free methods, achieving stronger alignment with edit prompts while preserving high-fidelity details in irrelevant regions. Our main contributions are summarized as follows:

- **Theoretical Foundation of FlowBypass:** We provide a rigorous mathematical formulation of inversion and reconstruction trajectories, and derive an approximate bypass solution with a tractable analytical form, laying the theoretical groundwork for FlowBypass.

- **Unified and Practical Realization:** We transform the

analytical solution into an efficient discretized form, yielding a unified training-free image editing framework based on Rectified Flow. It bridges theory and practice by bypassing inversion to directly guide reconstruction, removing the need for backbone-specific feature manipulations and improving both fidelity and alignment.

- **State-of-the-Art Performance:** Extensive experiments demonstrate that FlowBypass consistently achieves state-of-the-art results across challenging editing scenarios, delivering superior fidelity–alignment trade-offs and robust generalization compared to existing training-free methods.

2. Related Works

Training-free image editing aims to manipulate images without additional training or fine-tuning. Rather than updating model parameters (Brooks et al., 2023; Yu et al., 2025; Chen et al., 2025; Xiao et al., 2025), these methods directly exploit pre-trained generative models. Existing approaches can be broadly grouped into four categories according to how they modify the sampling process.

The most common paradigm is noise-inversion methods, the dominant paradigm where an original image is mapped into the noise space and then reconstructed into the edited result. Most build upon DDIM-inversion (Song et al., 2021), with modifications to inversion and reconstruction trajectories (Huberman-Spiegelglas et al., 2024; Mokady et al., 2023; Brack et al., 2024; Miyake et al., 2025), but they remain fundamentally constrained by accumulated errors, especially near the inverted noise. Recently, training-free editing has also been extended to Rectified Flow (RF) models (Wang et al., 2025; Rout et al., 2025), but most remain rooted in DDIM-based principles, which continue to suffer from the accumulation of trajectory errors.

The second paradigm is prompt- or condition-refinement, which enhances the conditioning signal by incorporating information from the source image, thereby enabling edits within the reconstruction trajectory (Ravi et al., 2023; Wang et al., 2023). The third paradigm is feature manipulation, where intermediate representations are modified either by injecting features from the inversion trajectory to improve fidelity or by amplifying prompt-related activations to strengthen alignment (Hertz et al., 2023; Tumanyan et al., 2023; Cao et al., 2023; Feng et al., 2025).

The fourth paradigm skips explicit inversion, using a coarse preliminary interception for pseudo-inversion and then operating directly in the image distribution, which is far more complex than the noise-blended domain (Xu et al., 2024; Kulikov et al., 2025). Consequently, inversion-free methods may introduce artifacts during editing, often resulting in degraded visual quality.

Despite their methodological diversity, most of these methods rely on full trajectory traversal, which inherently amplifies discretization errors and weak conditional guidance. As a result, training-free editing often introduces unintended modifications in irrelevant regions or even fails to realize the intended edit. This persistent bottleneck motivates the development of **FlowBypass**, a principled framework designed to mitigate accumulated errors while preserving both fidelity and alignment.

3. Method

3.1. Preliminaries

Rectified Flow (RF). RF formulates image generation as a continuous transformation of a Gaussian noise distribution $\mathcal{N}(0, \mathbf{I})$ into the target data distribution p_{data} under conditioning signals, governed by a velocity field expressed as an ordinary differential equation (ODE):

$$\frac{d}{dt} z_t = \bar{v}(z_t, t, C), \quad (1)$$

where $t \in [0, 1]$ is the continuous timestep, $z_0 \sim p_{\text{data}}$ is a real image, $z_1 = \epsilon \sim \mathcal{N}(0, \mathbf{I})$ is a Gaussian noise sample, \bar{v} is the marginal velocity field (Lipman et al., 2023), and C is the provided condition (e.g., text prompts). The RF network v_θ is trained to approximate the marginal velocity field \bar{v} by minimizing $\mathbb{E}_{t, z_0, \epsilon} \|v_\theta(z_t, t, C) - (\epsilon - z_0)\|^2$, where $z_t = t \cdot \epsilon + (1 - t) \cdot z_0$ is the linear interpolation of z_0 and ϵ . Sampling seeks to recover a clean image z_0 from noise ϵ using Euler discretization of Equ. 1, once the velocity field is well estimated by v_θ .

Classifier-Free Guidance (CFG). CFG is widely used to balance semantic alignment and visual fidelity during sampling. Given velocity fields predicted under a positive prompt C_p and a negative prompt C_n , the guided velocity field can be formulated as:

$$\hat{v}_\theta(z_t, t, C_p, C_n) = v_\theta(z_t, t, C_p) + \omega \cdot (v_\theta(z_t, t, C_p) - v_\theta(z_t, t, C_n)), \quad (2)$$

where ω is the guidance scale. The larger values of ω amplify the contribution of positive prompt, typically leading to improved semantic alignment with provided condition but at the risk of sacrificing diversity and visual fidelity. Substituting \hat{v}_θ into Equ. 1 yields the CFG-guided trajectory:

$$z_t = z_r + \int_r^t \hat{v}_\theta(z_\tau, \tau, C_p, C_n) d\tau. \quad (3)$$

Numerical Integration. The above ODEs can be solved numerically through discretization. Starting from $z_{t_N} = \epsilon \sim \mathcal{N}(0, \mathbf{I})$ at $t_N = 1$ and using a monotonic sequence of timesteps $\{t_0 = 0, t_1, \dots, t_N = 1\}$, Euler discretization updates the state as:

$$z_{t_{i-1}} = z_{t_i} + (t_{i-1} - t_i) \cdot \hat{v}_\theta(z_{t_i}, t_i, C_p, C_n). \quad (4)$$

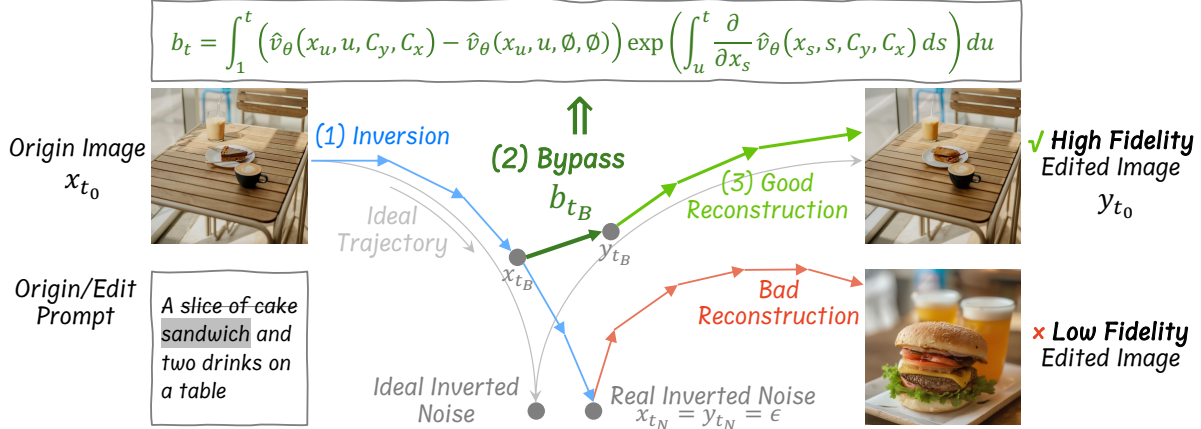


Figure 1. Framework of FlowBypass. FlowBypass consists of three steps: (1) Inverse the input image x_{t_0} with Euler discretization to obtain the inversion trajectory; (2) Calculate the bypass b_{t_B} using inversion trajectory according to Equ. 13; (3) Reconstruct from intermediate state $y_{t_B} = x_{t_B} + b_{t_B}$ to obtain edited image y_{t_0} . We show the differences between the origin prompt and the edit prompt by marking removed words with strikethrough and added words with gray background.

Iteratively applying Equ. 4, the initial noise gradually moves along the approximated trajectory until it reaches the final clean image z_{t_0} .

Inversion-based Image Editing. Given a pre-trained generative model \mathcal{M} , an input image x_{t_0} , and an origin condition C_x , the objective is to synthesize an edited image y_{t_0} that satisfies a user-specified edit condition C_y , while preserving the original content not related to the edit condition. The dominant pipeline consists of two stages: (i) *inversion*, mapping x_{t_0} into a corresponding Gaussian noise $x_{t_N} \equiv \epsilon \equiv y_{t_N}$ under the guidance of inversion condition C_{inv} ; and (ii) *reconstruction*, resampling from the noise y_{t_N} to reconstruct the edited image y_{t_0} under the guidance of reconstruction condition C_{rec} . The inversion and reconstruction trajectories share the same noise point $x_{t_N} \equiv \epsilon \equiv y_{t_N}$, while differing in their image points x_0 (origin image) and y_0 (edited image). While the design of C_{inv} and C_{rec} varies across methods, all such approaches depend on traversing the full inversion–reconstruction trajectory. This reliance makes them inherently vulnerable to numerical error accumulation and attenuated conditional guidance, which motivates the bypass strategy in our framework.

3.2. Motivation

A fundamental challenge in inversion-based training-free image editing is the progressive accumulation of errors during inversion and reconstruction. These errors in inversion primarily stem from two sources: (i) numerical discretization when solving the ODE in Equ. 4, and (ii) intrinsic mismatch between inversion and forward sampling. Concretely, the inversion equation $x_{t_i} = x_{t_{i-1}} + (t_i - t_{i-1}) \cdot \hat{v}_\theta(x_{t_i}, t_i, C_p, C_n)$ reformulated from Equ. 4 contains x_{t_i} on both sides, thereby necessitating an approximation

of $\hat{v}_\theta(x_{t_i}, t_i, C_p, C_n)$ with either $\hat{v}_\theta(x_{t_{i-1}}, t_i, C_p, C_n)$ or $\hat{v}_\theta(x_{t_{i-1}}, t_{i-1}, C_p, C_n)$. Such approximation introduces errors that propagate along the trajectory, ultimately yielding a degraded terminal state x_{t_N} . While the reconstruction trajectory is unaffected by intrinsic mismatch, it is still subject to errors caused by numerical discretization.

Our key insight is that fidelity loss in training-free editing is largely attributable to reconstructing from this corrupted terminal noise x_{t_N} . This observation motivates a departure from conventional designs: rather than relying on the error-prone endpoint, we propose to bypass it by selecting an intermediate state x_{t_B} , which preserves higher fidelity due to reduced error accumulation. We then construct the edited counterpart y_{t_B} by introducing a bypass term b_{t_B} , as illustrated in Fig. 1. This bypass enables a direct transition from inversion to reconstruction at t_B , effectively mitigating accumulated errors while ensuring semantic alignment with the edit prompt through b_{t_B} .

3.3. Formulation of FlowBypass

Given a pre-trained generative RF network v_θ , an origin image x_0 with its associated origin prompt C_x , and a target edit prompt C_y specifying the desired output y_0 , two ODEs can be established as:

$$\begin{aligned} x_t &= x_1 + \int_1^t \hat{v}_\theta(x_\tau, \tau, C_{inv}^p, C_{inv}^n) d\tau, \\ y_t &= y_1 + \int_1^t \hat{v}_\theta(y_\tau, \tau, C_{rec}^p, C_{rec}^n) d\tau, \end{aligned} \quad (5)$$

where C_{inv}^p and C_{inv}^n are the positive and negative prompts that control the inversion trajectory, and C_{rec}^p and C_{rec}^n control the reconstruction trajectory. The specific choice of these prompts is detailed in Sec. 3.4. We define the bypass

b_t as the offset between the two trajectories:

$$\begin{aligned} b_t &= y_t - x_t \\ &= \int_1^t \left(\hat{v}_\theta(y_\tau, \tau, C_{rec}^p, C_{rec}^n) - \hat{v}_\theta(x_\tau, \tau, C_{inv}^p, C_{inv}^n) \right) d\tau. \end{aligned} \quad (6)$$

Differentiating both sides with respect to t , which leads to:

$$\begin{aligned} \frac{d}{dt} b_t &= \hat{v}_\theta(y_t, t, C_{rec}^p, C_{rec}^n) - \hat{v}_\theta(x_t, t, C_{inv}^p, C_{inv}^n) \\ &= \hat{v}_\theta(x_t + b_t, t, C_{rec}^p, C_{rec}^n) - \hat{v}_\theta(x_t, t, C_{inv}^p, C_{inv}^n). \end{aligned} \quad (7)$$

Since b_t can be regarded as a small offset, so that the first term $\hat{v}_\theta(x_t + b_t, t, C_{rec}^p, C_{rec}^n)$ can be approximated with First-Order Taylor Expansion Formula:

$$\begin{aligned} \hat{v}_\theta(x_t + b_t, t, C_{rec}^p, C_{rec}^n) &\approx \hat{v}_\theta(x_t, t, C_{rec}^p, C_{rec}^n) + P_t \cdot b_t, \\ P_t &= \frac{\partial}{\partial x_t} \hat{v}_\theta(x_t, t, C_{rec}^p, C_{rec}^n). \end{aligned} \quad (8)$$

Substituting Equ. 8 into Equ. 7 yields an approximate linear ODE for b_t :

$$\begin{aligned} b_t &\approx b_t^*, b_t^* = 0, \\ \frac{d}{dt} b_t^* &= Q_t + P_t \cdot b_t^*, \\ Q_t &= \hat{v}_\theta(x_t, t, C_{rec}^p, C_{rec}^n) - \hat{v}_\theta(x_t, t, C_{inv}^p, C_{inv}^n), \end{aligned} \quad (9)$$

where b_t^* is an approximated b_t , and P_t is defined in Equ. 8. Equ. 9 is a first-order homogeneous linear differential equation, whose analytical solution is:

$$b_t^* = \int_1^t Q_u \exp\left(\int_u^t P_s ds\right) du, \quad (10)$$

where Q_u is defined in Equ. 9 and P_s is defined in Equ. 8.

This closed-form characterization of b_t^* provides a principled means of estimating the bypass term. Rather than depending on error-prone terminal inversion states, FlowBypass analytically derives an offset that directly links inversion and reconstruction at any intermediate time t . This formulation alleviates accumulated discretization errors, ensuring fidelity in irrelevant regions and alignment with edit prompts, while remaining agnostic to backbone architectures, thereby providing a general and powerful framework for training-free image editing.

3.4. Implementation of FlowBypass

Since Equ. 3 and Equ. 10 involve integral calculations, Euler discretization is employed in the inversion, bypass calculation, and reconstruction to obtain numerical solutions. Following Stable Diffusion 3.5 (Esser et al., 2024) and FLUX.1-dev (Batifol et al., 2025), we discretize the continuous time

interval $[0, 1]$ into a series of $N+1$ timesteps $\{t_0, t_1, \dots, t_N\}$, such that $t_i = \frac{\sigma i}{N + (\sigma - 1)i}$ with shift factor $\sigma = 3$.

Inversion. We first invert the origin image x_{t_0} with null prompt \emptyset , preserving sufficient structural information for subsequent reconstruction. The discretized inversion trajectory is obtained by:

$$x_{t_{i+1}} = x_{t_i} + (t_{i+1} - t_i) \cdot \hat{v}_\theta(x_{t_i}, t_i, C_{inv}^p, C_{inv}^n), \quad (11)$$

where the factor $(t_{i+1} - t_i) > 0$ pushes the state towards noise. Meanwhile, the terms $\hat{v}_\theta(x_{t_i}, t_i, C_{rec}^p, C_{rec}^n)$ and $\frac{\partial}{\partial x_{t_i}} \hat{v}_\theta(x_{t_i}, t_i, C_{rec}^p, C_{rec}^n)$ are also calculated, preparing the calculation of bypass b_t^* . Specifically, we set $C_{rec}^p = C_y$ (i.e., target edit prompt) and $C_{rec}^n = C_x$ (i.e., origin prompt) in the reconstruction trajectory. Importantly, our prompt choice is not an empirical hyperparameter decision but follows directly from the theoretical derivation of the bypass. The detail explanation will be given in Sec. 4.4.3.

The precise calculation of partial derivative $\frac{\partial}{\partial x_{t_i}} \hat{v}_\theta$ is computationally prohibitive for large-scale backbones. We approximate it via finite differences:

$$\frac{\partial}{\partial x_{t_i}} \hat{v}_\theta(x_{t_i}, t_i, C_y, C_x) \approx \frac{\hat{v}_\theta(x_{t_i} + \zeta, t_i, C_y, C_x) - \hat{v}_\theta(x_{t_i}, t_i, C_y, C_x)}{\zeta}, \quad (12)$$

where ζ is a small positive offset. This lightweight approximation introduces negligible bias while avoiding prohibitive memory and compute costs.

Bypass Calculation. We compute the bypass b_t using the trapezoidal variant of Euler discretization applied to Equ. 10:

$$\begin{aligned} b_{t_i}^* &\approx -\frac{1}{2} \sum_{u=i}^{N-1} (t_{u+1} - t_u) \cdot (Q'_u \cdot E'_u + Q'_{u+1} \cdot E'_{u+1}), \\ Q'_u &= \hat{v}_\theta(x_{t_u}, t_u, C_y, C_x) - \hat{v}_\theta(x_{t_u}, t_u, \emptyset, \emptyset), \\ E'_u &= \Gamma\left(-\frac{1}{2} \sum_{s=i}^{u-1} (t_{s+1} - t_s) \cdot (P'_s + P'_{s+1})\right), \\ P'_s &= \frac{\hat{v}_\theta(x_{t_s} + \zeta, t_s, C_y, C_x) - \hat{v}_\theta(x_{t_s}, t_s, C_y, C_x)}{\zeta}, \\ \Gamma(x) &= \begin{cases} \exp(x), x \leq 0 \\ x + 1, x > 0 \end{cases}. \end{aligned} \quad (13)$$

To stabilize numerical evaluation, we replace the exponential with its first-order Taylor approximation in the positive domain, preventing uncontrolled growth.

Reconstruction. Unlike prior inversion–reconstruction pipelines, FlowBypass constructs the reconstruction trajectory starting from an intermediate state y_{t_B} , rather than from

Table 1. Comparison with state-of-the-art image editing methods. OR denotes Optimization-Required, FM denotes Feature-Manipulation, SD is Stable Diffusion, LCM v7 is LCM Dreamshaper v7. Red, green, and blue highlight the best, second-best, and third-best results, respectively. The * marks indicate that the official code lacks real-image editing implementations, so we implement them ourselves following the authors’ guidance.

Method	Backbone	OR?	FM?	LPIPS↓	I.Sim.↑	T.Sim.↑
P2P* (Hertz et al., 2023)	SD1.4	No	Yes	0.4990	81.04	26.93
NTI (Mokady et al., 2023)	SD1.4	Yes	Yes	0.5798	73.96	26.38
DDCM (Xu et al., 2024)	LCM v7	No	Yes	0.4507	87.14	26.62
IP2P (Brooks et al., 2023)	SD1.4	Yes	No	0.6103	84.85	23.95
Omni-Gen (Xiao et al., 2025)	Phi-3	Yes	No	0.3573	87.48	25.58
LEDITS++ (Brack et al., 2024)	SD 1.5	No	Yes	0.3554	81.54	21.73
RF-Solver (Wang et al., 2025)	FLUX.1-dev	No	Yes	0.3880	87.32	25.30
RF-Inversion (Rout et al., 2025)	FLUX.1-dev	No	No	0.5659	83.35	25.71
FluxSpace* (Dalva et al., 2025)	FLUX.1-dev	No	Yes	0.8058	79.74	22.74
FireFlow (Deng et al., 2025)	FLUX.1-dev	No	Yes	0.3850	87.01	25.69
FlowEdit (Kulikov et al., 2025)	FLUX.1-dev	No	No	0.3921	87.90	25.28
FlowBypass	SD3.5 Medium	No	No	0.4228	85.96	26.45
FlowBypass	SD3.5 Large	No	No	0.4507	84.73	27.09
FlowBypass	FLUX.1-dev	No	No	0.3425	88.06	25.65

the inverted noise y_{t_N} . The reconstruction trajectory can be described as:

$$\begin{aligned} y_{t_B} &= x_{t_B} + b_{t_B}, \\ y_{t_{i-1}} &= y_{t_i} + (t_{i-1} - t_i) \cdot \hat{v}_\theta(y_{t_i}, t_i, C_y, C_x), \end{aligned} \quad (14)$$

where B is a user-specified bypass timestep between 0 and N , the factor $(t_{i-1} - t_i) < 0$ pushes the noisy state to the edit image y_{t_0} . A larger B prioritizes alignment with the edit prompt, while a smaller B favors fidelity to the original image. The solved y_{t_0} corresponds to the desired edited image.

4. Experiments

In this section, we present a comprehensive evaluation of our approach. Through both qualitative and quantitative analyses, we demonstrate the effectiveness and superiority of our approach. Furthermore, we conduct ablation studies to evaluate the contribution of each component in our design, including backbone robustness, approximation, and prompt choice, while the ablation studies of CFG scale, bypass step, and hyperparameter ζ are provided in the Appendix.

4.1. Experiment Setups

Baselines, Datasets, and Metrics. We compare FlowBypass against diverse state-of-the-art baselines, including DDIM-based approaches such as NTI (Mokady et al., 2023), DDCM (Xu et al., 2024), IPix2Pix (Brooks et al., 2023), Omni-Gen (Xiao et al., 2025), and LEDITS++ (Brack et al., 2024), as well as RF-based methods including RF-Solver (Wang et al., 2025), RF-Inversion (Rout et al., 2025),

FluxSpace (Dalva et al., 2025), FireFlow (Deng et al., 2025) and FlowEdit (Kulikov et al., 2025).

For evaluation, we adopt the EditEvalv2 benchmark (Huang et al., 2025), which contains 150 high-resolution images across seven sub-tasks: object addition, object replacement, object removal, background change, style change, texture change, and action change. Each image is resized while preserving its aspect ratio, with the longer side scaled to 1024 pixels for computational efficiency.

We assess editing performance from three complementary perspectives: (i) *perceptual fidelity*, measured by LPIPS (Zhang et al., 2018) between edited and original images; (ii) *semantic fidelity*, quantified by CLIP similarity (Radford et al., 2021) between edited and original images (*i.e.*, I.Sim.); and (iii) *semantic alignment*, evaluated by CLIPS (Hessel et al., 2021) between edited images and edit prompts (*i.e.*, T.Sim.).

Implementation Details. FlowBypass is implemented in PyTorch and all experiments are conducted on a single NVIDIA GeForce RTX 4090 GPU. We evaluate on three widely used RF backbones: Stable Diffusion 3.5 Medium (*i.e.*, SD3.5M), Stable Diffusion 3.5 Large (*i.e.*, SD3.5L) (Esser et al., 2024), and FLUX.1-dev (*i.e.*, FLUX) (Batifol et al., 2025).

4.2. Quantitative Comparison with State-of-the-Art Methods

We quantitatively compare FlowBypass with existing editing methods in Tab. 1. The * marks indicate that the official codebase does not provide implementations for real-image

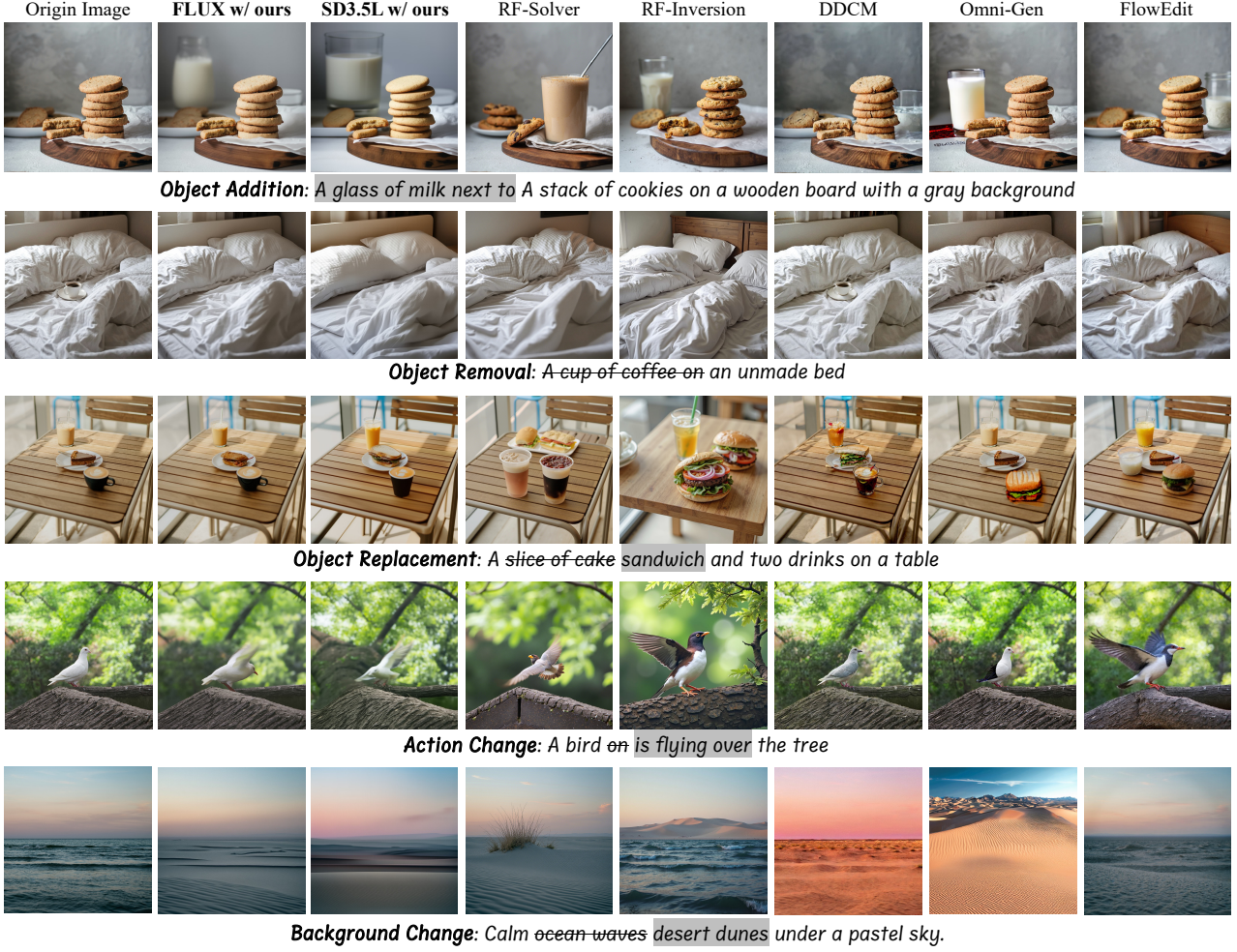


Figure 2. Qualitative comparison with other image editing methods. Zoom in for a better view.

Table 2. Performance of different backbones.

Backbone	Setting	LPIPS. \downarrow	I.Sim. \uparrow	T.Sim. \uparrow
SD3.5M	w/ FlowBypass	0.4228	85.96	26.45
	Rec. from t=30	0.3082	90.67	24.87
	Rec. from t=50	0.6354	77.18	27.57
SD3.5L	w/ FlowBypass	0.4507	84.73	27.09
	Rec. from t=30	0.3288	91.01	25.36
	Rec. from t=50	0.6576	76.95	27.94
FLUX	w/ FlowBypass	0.3425	88.06	25.65
	Rec. from t=30	0.2240	94.47	23.85
	Rec. from t=50	0.5811	78.21	27.78

editing. Therefore, we implement these components ourselves following the authors' guidelines. Importantly, superior editing performance cannot be judged by fidelity or alignment in isolation; an effective method must achieve a favorable balance across both dimensions. As reported

in Tab. 1, FLUX w/ FlowBypass achieves the highest perceptual fidelity, while SD3.5L w/ FlowBypass demonstrates the best semantic alignment. More importantly, across all three backbones, FlowBypass consistently delivers strong alignment without substantially compromising fidelity. This trend is clearly reflected in Fig. 3, where the FlowBypass-related points are positioned closest to the top-left corner, approaching the Pareto frontier of fidelity and alignment. These results confirm the effectiveness of FlowBypass in achieving superior image editing performance with high fidelity and alignment.

4.3. Qualitative Comparison with State-of-the-Art Editing Methods

The qualitative comparison with state-of-the-art image editing baselines is presented in Fig. 2. To assess the versatility of different approaches, we evaluate their performance across diverse sub-tasks. Baseline methods often exhibit undesired modifications or incomplete edits, for example,

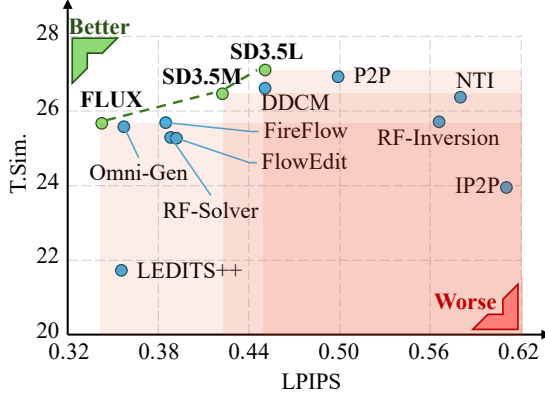


Figure 3. Scatter figure of quantitative comparison. Green points denote the performance of FlowBypass, whereas blue points denote the performance of other methods. FluxSpace is omitted because its extremely poor performance would compromise the readability of the scatter plot.

unintentionally altering coffee cups in the Object Replacement sub-task or failing to animate the bird in the Action Change sub-task. In contrast, FlowBypass consistently delivers edits that closely follow the intended prompts while preserving structural and textural fidelity in regions that should remain untouched. This balance between alignment and fidelity underscores the robustness of FlowBypass and highlights its superior editing capability. More qualitative comparison and edited results outside the EditEvalv2 dataset are provided in the Appendix. We also conduct a user study to provide comprehensive subjective evidence of the visual performance of our method in the Appendix.

4.4. Ablation Study

4.4.1. ROBUSTNESS ON DIFFERENT BACKBONES

We perform an ablation study to evaluate the robustness of FlowBypass across three representative different backbones, including SD3.5M, SD3.5L, and FLUX. As mentioned before, the reconstruction trajectory starts from $y_{t_B} = x_{t_B} + b_{t_B}$. To verify the alignment contributed by FlowBypass, we conduct two diagnostic settings: (i) we set $b_{t_B} = 0$ and reconstruct from timestep $t = 30$, denoted as ‘‘Rec. from $t = 30$ ’’; and (ii) we execute the entire reconstruction trajectory, starting from $t = 50$, to examine the fidelity from FlowBypass, denoted as ‘‘Rec. from $t = 50$ ’’.

As shown in Tab. 2, reconstructing the entire trajectory from $t = 50$ degrades fidelity due to error accumulation, whereas disabling the bypass at $t = 30$ limits the framework’s ability to perform effective edits in response to the edit prompts. In practice, reconstruction from $t = 30$ results in under-edited outputs, while starting from $t = 50$ introduces unintended changes, as illustrated by the qualitative results provided in the Appendix. In contrast, the proposed FlowBypass incor-

Table 3. Effectiveness of Approximation.

Backbone	Setting	LPIPS↓	I.Sim.↑	T.Sim.↑
SD3.5L	w/o FlowBypass	0.3288	91.01	25.36
	w/o Approx. $\frac{\partial}{\partial x_{t_i}} \hat{v}_\theta$	0.4035	86.67	26.73
	w/o Approx. exp	0.5719	78.12	26.22
	w/ FlowBypass	0.4507	84.73	27.09
FLUX	w/o FlowBypass	0.2240	94.47	23.85
	w/o Approx. $\frac{\partial}{\partial x_{t_i}} \hat{v}_\theta$	0.3013	89.98	25.38
	w/o Approx. exp	0.4188	85.17	25.57
	w/ FlowBypass	0.3425	88.06	25.65

porates an appropriate bypass b_{t_B} , enabling faithful and accurate editing that achieves a better balance between fidelity and alignment across different backbones. The visualization in Fig. 4 further confirms that bypasses exhibit strong activations in the regions specified by the edit prompts, while remaining low in irrelevant areas that should stay consistent with the original images.

4.4.2. EFFECTIVENESS OF APPROXIMATION

We conduct an ablation study to evaluate the effectiveness of the approximations in Equ. 12 and Equ. 13. Since precisely computing the gradient is intractable, we set $\frac{\partial}{\partial x_{t_i}} \hat{v}_\theta$ in Equ. 12 to zero to assess the contribution of the gradient term in the bypass. In addition, we perform ablation experiments on the approximation of exp in Equ. 13 to examine its role in avoiding numerical instability. The results summarized in Tab. 3 indicate that approximating $\frac{\partial}{\partial x_{t_i}} \hat{v}_\theta$ leads to improved alignment, while introducing the approximation of exp further enhances both fidelity and alignment. We observe that neglecting the gradient approximation introduces unrealistic local structures, whereas omitting the approximation of exp leads to uncontrolled exponential growth, which results in severe artifacts in the edited images. More example outputs are provided in the Appendix.

4.4.3. IMPACT OF PROMPT CHOICE

The choice of prompts plays a crucial role in FlowBypass. As shown in Equ. 10, four prompts need to be determined: C_{inv}^p , C_{inv}^n , C_{rec}^p , and C_{rec}^n . To explore this design, we evaluate different reasonable prompt combinations, with results illustrated in Fig. 5. The detailed statistical results and qualitative comparison are provided in the Appendix.

Among them, the combination ‘‘ee/yx’’ which applies the empty prompt \emptyset during inversion and uses C_y as the positive prompt and C_x as the negative prompt during reconstruction achieves the best balance between fidelity and alignment. We attribute this to two factors: (i) using the empty prompt \emptyset in inversion preserves sufficient structural and se-

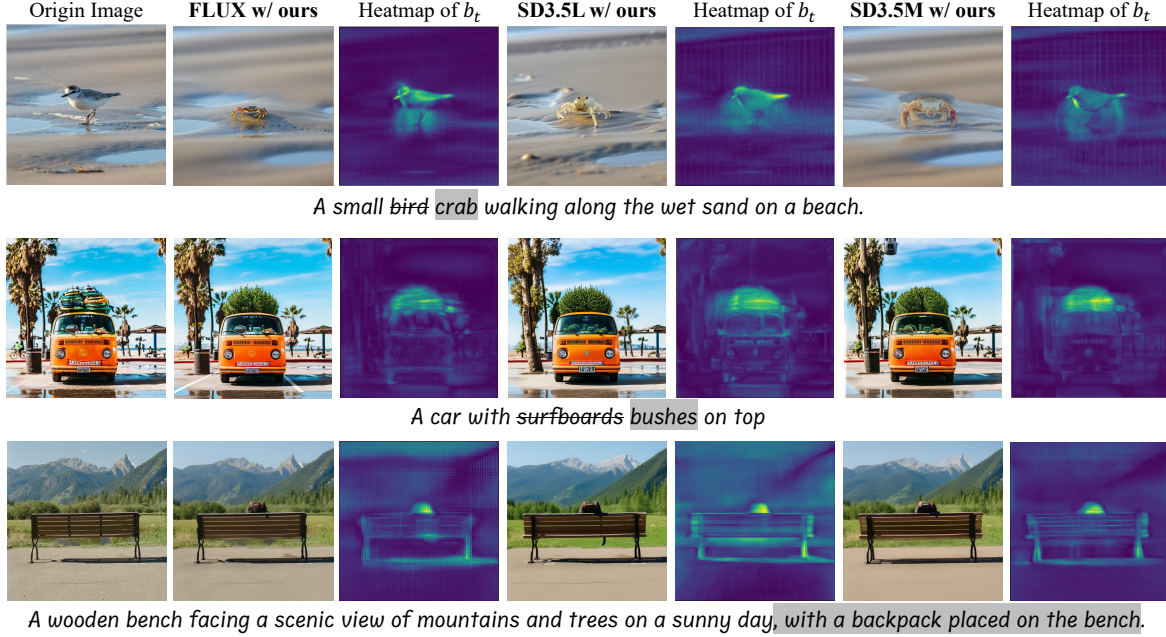


Figure 4. Visualization of bypass. Yellow regions indicate higher L1-norm values, while blue regions indicate lower values, reflecting the spatial distribution of bypass magnitude. Zoom in for a better view.

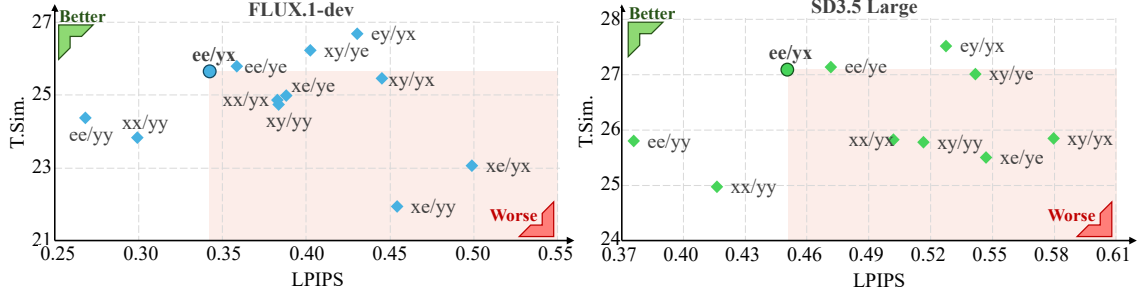


Figure 5. Performance of different prompt choices. In each notation, the segment before the slash denotes inversion prompts and the segment after the slash denotes reconstruction prompts. Within each segment, the first character indicates the positive prompt and the second indicates the negative prompt, where “x” denotes C_x , “y” denotes C_y , and “e” denotes \emptyset .

semantic information from the origin images in the inversion trajectory, thus benefiting fidelity; and (ii) the balanced nonlinear compensation constructed by $C_{rec}^p = C_y, C_{rec}^n = C_x$. Specifically, in the analytical solution of a first-order linear differential equation, the exponential term acts as the accumulated effect of nonlinear terms along the trajectory. In FlowBypass, this exponential term compensates for the semantic discrepancies introduced by the Taylor expansion. Consequently, using the “yx” prompt configuration provides a balanced compensation for this integrating term and amplifies the semantic shift from origin semantics to edit semantics. Alternative settings (e.g., “ye” and “yy”) would create an imbalanced compensation, causing the bypass computation to overly favor either the target or the origin image, thereby harming fidelity or alignment.

5. Conclusion

In this work, we propose FlowBypass, a general rectified-flow image editing framework that achieves high alignment with target edit prompts while preserving consistency with irrelevant regions of the original images. It is accomplished by introducing a bypass between the inversion and reconstruction trajectories, without requiring any additional training, test-time optimization, or feature manipulation. The framework is theoretically motivated by the formulation of bypassing across two trajectories and is realized through carefully designed approximations and prompt selection strategies. Extensive experiments demonstrate that FlowBypass outperforms existing state-of-the-art methods, striking a superior balance between fidelity and alignment.

Impact Statement

This paper presents work whose goal is to advance the field of machine learning. There are many potential societal consequences of our work, none of which we feel must be specifically highlighted here.

References

Batifol, S., Blattmann, A., Boesel, F., Consul, S., Diagne, C., Dockhorn, T., English, J., English, Z., Esser, P., Kulal, S., et al. Flux. 1 kontext: Flow matching for in-context image generation and editing in latent space. *arXiv preprint arXiv:2506.15742*, 2025.

Brack, M., Friedrich, F., Kornmeier, K., Tsaban, L., Schramowski, P., Kersting, K., and Passos, A. Ledits++: Limitless image editing using text-to-image models. In *Proceedings of the IEEE/CVF Conference on Computer Vision and Pattern Recognition*, pp. 8861–8870, 2024.

Brooks, T., Holynski, A., and Efros, A. A. Instructpix2pix: Learning to follow image editing instructions. In *Proceedings of the IEEE/CVF Conference on Computer Vision and Pattern Recognition*, pp. 18392–18402, 2023.

Cao, M., Wang, X., Qi, Z., Shan, Y., Qie, X., and Zheng, Y. Masactrl: Tuning-free mutual self-attention control for consistent image synthesis and editing. In *Proceedings of 2023 IEEE/CVF International Conference on Computer Vision*, pp. 22503–22513, 2023.

Chen, X., Zhang, Z., Zhang, H., Zhou, Y., Kim, S. Y., Liu, Q., Li, Y., Zhang, J., Zhao, N., Wang, Y., et al. Unireal: Universal image generation and editing via learning real-world dynamics. In *Proceedings of the Computer Vision and Pattern Recognition Conference*, pp. 12501–12511, 2025.

Dalva, Y., Venkatesh, K., and Yanardag, P. Fluxspace: Disentangled semantic editing in rectified flow models. In *Proceedings of the Computer Vision and Pattern Recognition Conference*, pp. 13083–13092, 2025.

Deng, Y., He, X., Mei, C., Wang, P., and Tang, F. Fireflow: Fast inversion of rectified flow for image semantic editing. In *Proceedings of International Conference on Machine Learning*, 2025.

Esser, P., Kulal, S., Blattmann, A., Entezari, R., Müller, J., Saini, H., Levi, Y., Lorenz, D., Sauer, A., Boesel, F., et al. Scaling rectified flow transformers for high-resolution image synthesis. In *Proceedings of Forty-first International Conference on Machine Learning*, 2024.

Feng, K., Ma, Y., Wang, B., Qi, C., Chen, H., Chen, Q., and Wang, Z. Dit4edit: Diffusion transformer for image editing. In *Proceedings of the AAAI Conference on Artificial Intelligence*, volume 39, pp. 2969–2977, 2025.

Hertz, A., Mokady, R., Tenenbaum, J. M., Aberman, K., Pritch, Y., and Cohen-Or, D. Prompt-to-prompt image editing with cross attention control. In *Proceedings of the International Conference on Learning Representations*, 2023.

Hessel, J., Holtzman, A., Forbes, M., Bras, R. L., and Choi, Y. Clipscore: A reference-free evaluation metric for image captioning. *arXiv preprint arXiv:2104.08718*, 2021.

Huang, Y., Huang, J., Liu, Y., Yan, M., Lv, J., Liu, J., Xiong, W., Zhang, H., Cao, L., and Chen, S. Diffusion model-based image editing: A survey. *IEEE Transactions on Pattern Analysis and Machine Intelligence*, 2025.

Huberman-Spiegelglas, I., Kulikov, V. B., and Michaeli, T. An edit friendly ddpm noise space: Inversion and manipulations. In *Proceedings of the IEEE/CVF Conference on Computer Vision and Pattern Recognition*, pp. 12469–12478, 2024.

Kulikov, V., Kleiner, M., Huberman-Spiegelglas, I., and Michaeli, T. Flowedit: Inversion-free text-based editing using pre-trained flow models. In *Proceedings of the IEEE/CVF International Conference on Computer Vision*, pp. 19721–19730, 2025.

Lipman, Y., Chen, R. T., Ben-Hamu, H., Nickel, M., and Le, M. Flow matching for generative modeling. In *Proceedings of the International Conference on Learning Representations*, 2023.

Liu, X., Gong, C., et al. Flow straight and fast: Learning to generate and transfer data with rectified flow. In *Proceedings of the International Conference on Learning Representations*, 2022.

Miyake, D., Iohara, A., Saito, Y., and Tanaka, T. Negative-prompt inversion: Fast image inversion for editing with text-guided diffusion models. In *2025 IEEE/CVF Winter Conference on Applications of Computer Vision*, pp. 2063–2072. IEEE, 2025.

Mokady, R., Hertz, A., Aberman, K., Pritch, Y., and Cohen-Or, D. Null-text inversion for editing real images using guided diffusion models. In *Proceedings of the IEEE/CVF Conference on Computer Vision and Pattern Recognition*, pp. 6038–6047, 2023.

Radford, A., Kim, J. W., Hallacy, C., Ramesh, A., Goh, G., Agarwal, S., Sastry, G., Askell, A., Mishkin, P., Clark, J., et al. Learning transferable visual models from natural language supervision. In *Proceedings of International Conference on Machine Learning*, pp. 8748–8763, 2021.

Rajbhandari, S., Rasley, J., Ruwase, O., and He, Y. Zero: Memory optimizations toward training trillion parameter models. In *SC20: International Conference for High Performance Computing, Networking, Storage and Analysis*, pp. 1–16. IEEE, 2020.

Ravi, H., Kelkar, S., Harikumar, M., and Kale, A. Predictor: Text guided image editing with diffusion prior. *ArXiv*, abs/2302.07979, 2023.

Rout, L., Chen, Y., Ruiz, N., Caramanis, C., Shakkottai, S., and Chu, W.-S. Semantic image inversion and editing using rectified stochastic differential equations. In *Proceedings of the International Conference on Learning Representations*, 2025.

Simsar, E., Tonioni, A., Xian, Y., Hofmann, T., and Tombari, F. Lime: localized image editing via attention regularization in diffusion models. In *2025 IEEE/CVF Winter Conference on Applications of Computer Vision*, pp. 222–231. IEEE, 2025.

Song, J., Meng, C., and Ermon, S. Denoising diffusion implicit models. In *Proceedings of the International Conference on Learning Representations*, 2021.

Timofte, R. and Agustsson, E. Ntire 2017 challenge on single image super-resolution: Methods and results. In *Proceedings of IEEE Conference on Computer Vision and Pattern Recognition Workshops*, pp. 1110–1121, 2017.

Tumanyan, N., Geyer, M., Bagon, S., and Dekel, T. Plug-and-play diffusion features for text-driven image-to-image translation. In *Proceedings of the IEEE/CVF Conference on Computer Vision and Pattern Recognition*, pp. 1921–1930, 2023.

Wang, J., Pu, J., Qi, Z., Guo, J., Ma, Y., Huang, N., Chen, Y., Li, X., and Shan, Y. Taming rectified flow for inversion and editing. In *Proceedings of the International Conference on Machine Learning*, 2025.

Wang, Q., Zhang, B., Birsak, M., and Wonka, P. Instructedit: Improving automatic masks for diffusion-based image editing with user instructions. *arXiv preprint arXiv:2305.18047*, 2023.

Xiao, S., Wang, Y., Zhou, J., Yuan, H., Xing, X., Yan, R., Li, C., Wang, S., Huang, T., and Liu, Z. Omnigen: Unified image generation. In *Proceedings of the Computer Vision and Pattern Recognition Conference*, pp. 13294–13304, 2025.

Xu, S., Huang, Y., Pan, J., Ma, Z., and Chai, J. Inversion-free image editing with language-guided diffusion models. In *Proceedings of the IEEE/CVF Conference on Computer Vision and Pattern Recognition*, pp. 9452–9461, 2024.

Yu, Q., Chow, W., Yue, Z., Pan, K., Wu, Y., Wan, X., Li, J., Tang, S., Zhang, H., and Zhuang, Y. Anyedit: Mastering unified high-quality image editing for any idea. In *Proceedings of the Computer Vision and Pattern Recognition Conference*, pp. 26125–26135, 2025.

Zhang, R., Isola, P., Efros, A. A., Shechtman, E., and Wang, O. The unreasonable effectiveness of deep features as a perceptual metric. In *Proceedings of the IEEE Conference on Computer Vision and Pattern Recognition*, pp. 586–595, 2018.

Appendix

A. Solving of ODE

The ODE described in Equ. 9 can be solved using the Integrating Factor Method. Equ. 9 can be rewritten as:

$$\begin{aligned} \frac{d}{dt} b_t^* &= Q(t) + P(t) \cdot b_t^*, \\ Q(t) &= \hat{v}_\theta(x_t, t, C_{rec}^p, C_{rec}^n) - \hat{v}_\theta(x_t, t, C_{inv}^p, C_{inv}^n), \\ P(t) &= \frac{\partial}{\partial x_t} \hat{v}_\theta(x_t, t, C_{rec}^p, C_{rec}^n), \\ b_1^* &= 0. \end{aligned} \tag{15}$$

Let

$$\mu(t) = \exp \left(- \int_1^t P(s) ds \right), \tag{16}$$

and it can be obtained that

$$\frac{d}{dt} [\mu(t) b_t^*] = \mu(t) \frac{d}{dt} b_t^* - \mu(t) P(t) b_t^* = \mu(t) Q(t). \tag{17}$$

Integrating both sides of the equation with respect to t from 1 yields:

$$\mu(t) b_t^* - \mu(1) b_1^* = \int_1^t \mu(u) Q(u) du. \tag{18}$$

Due to $b_1^* = 0$ and $\mu(t) > 0$ for any t , Equ. 18 can be rearranged as:

$$\begin{aligned} b_t^* &= \frac{\int_1^t \mu(u) Q(u) du + 0}{\mu(t)} \\ &= \exp \left(\int_1^t P(s) ds \right) \int_1^t \exp \left(- \int_1^u P(s) ds \right) Q(u) du \\ &= \int_1^t \exp \left(\int_1^t P(s) ds - \int_1^u P(s) ds \right) Q(u) du \\ &= \int_1^t \exp \left(\int_u^t P(s) ds \right) Q(u) du \\ &= \int_1^t \left(\hat{v}_\theta(x_u, u, C_{rec}^p, C_{rec}^n) - \hat{v}_\theta(x_u, u, C_{inv}^p, C_{inv}^n) \right) \exp \left(\int_u^t \frac{\partial}{\partial x_s} \hat{v}_\theta(x_s, s, C_{rec}^p, C_{rec}^n) ds \right) du, \end{aligned} \tag{19}$$

which is equal to Equ. 10.

B. Additional Experiment Results

B.1. Detailed Statistical Analysis of Ablation on Prompt Choice

The detailed statistical results of Fig. 5 in main text is demonstrated in Tab. 4. Besides, we provide the visual comparison with different prompt choices in Fig. 6, which indicates that the combination “ee/yx” preserves the fidelity of irrelevant regions while successfully applying the intended edit.

B.2. Visualization of Approximation

Fig. 7 shows the ablation results on approximation. Severe artifacts appear when the approximation of \exp is omitted, as illustrated in the fourth and seventh columns. We argue that these artifacts mainly arise from exponential explosion, which

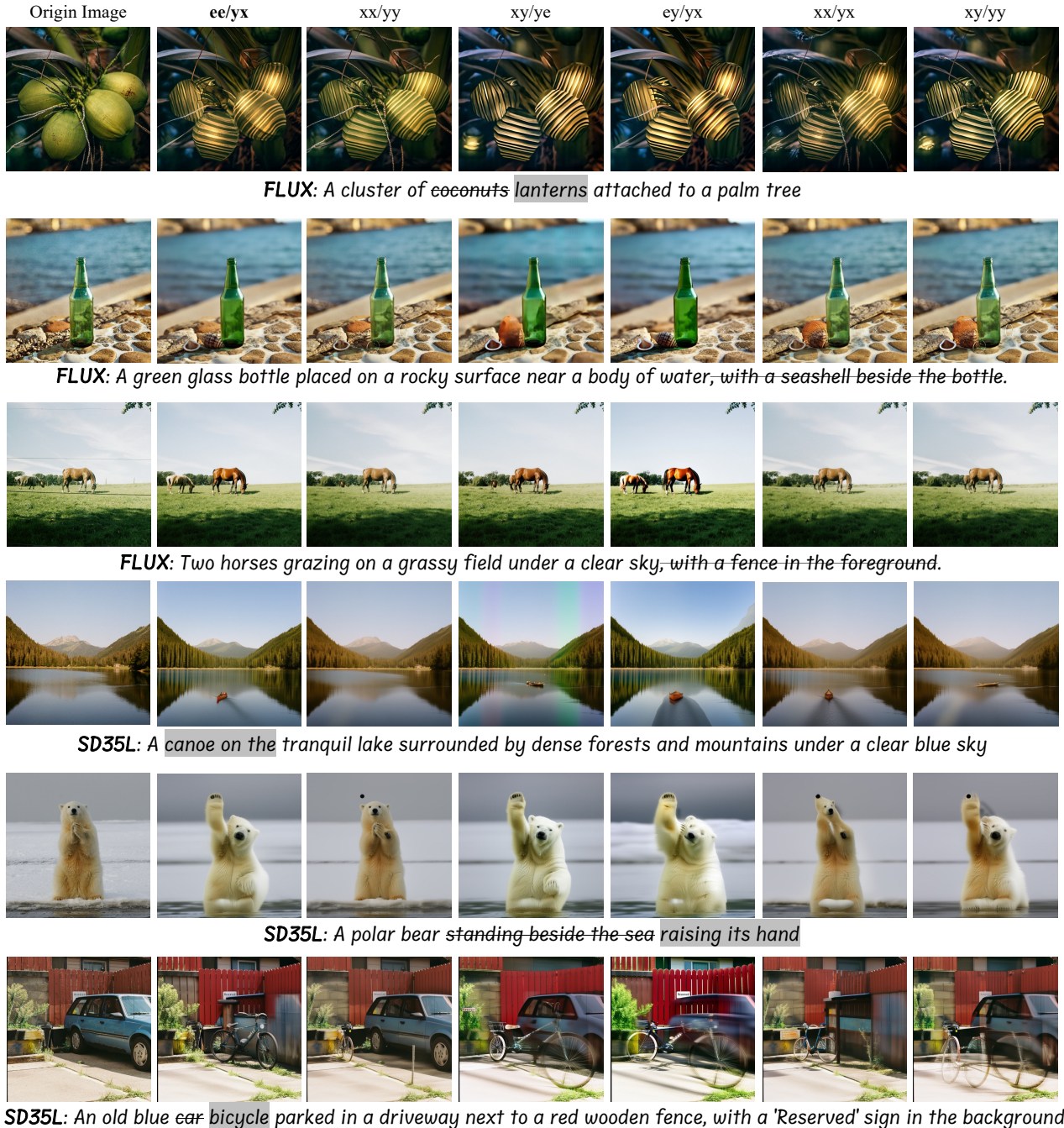


Figure 6. Visual comparison of ablation results on different prompt choices. Zoom in for a better view.

Table 4. Impact of Prompt Choice.

Backbone		FLUX.1-dev			SD3.5 Large		
Inverse	Edit	LPIPS↓	I.Sim.↑	T.Sim.↑	LPIPS↓	I.Sim.↑	T.Sim.↑
(+ C_x , - C_y)	(+ C_y , - C_x)	0.4454	83.41	25.47	0.5798	77.58	25.85
(+ C_x , - C_y)	(+ C_y , - \emptyset)	0.4024	86.07	26.23	0.5418	81.25	27.01
(+ C_x , - C_y)	(+ C_y , - C_y)	0.3836	86.54	24.74	0.5166	81.04	25.78
(+ C_x , - \emptyset)	(+ C_y , - C_x)	0.4990	79.11	23.07	0.7083	68.29	20.01
(+ C_x , - \emptyset)	(+ C_y , - \emptyset)	0.3881	86.19	24.99	0.5471	79.72	25.50
(+ C_x , - \emptyset)	(+ C_y , - C_y)	0.4542	82.28	21.95	0.6834	69.48	18.79
(+ C_x , - C_x)	(+ C_y , - C_y)	0.2992	90.85	23.84	0.4163	87.15	24.98
(+ C_x , - C_x)	(+ C_y , - C_x)	0.3828	86.10	24.87	0.5022	81.40	25.83
(+ \emptyset , - C_y)	(+ C_y , - C_x)	0.4305	85.66	26.69	0.5277	82.46	27.52
(+ \emptyset , - \emptyset)	(+ C_y , - C_y)	0.2685	93.16	24.38	0.3759	90.00	25.80
(+ \emptyset , - \emptyset)	(+ C_y , - \emptyset)	0.3586	89.65	25.80	0.4716	85.55	27.14
(+ \emptyset , - \emptyset)	(+ C_y , - C_x)	0.3425	88.06	25.65	0.4507	84.73	27.09

Table 5. Impact of CFG scale.

Backbone		FLUX.1-dev			SD3.5 Large		
CFG scale	LPIPS↓	I.Sim.↑	T.Sim.↑	LPIPS↓	I.Sim.↑	T.Sim.↑	
1.5	0.3036	90.55	25.23	0.4155	87.04	26.83	
2.0	0.3425	88.06	25.65	0.4507	84.73	27.09	
2.5	0.3731	86.55	26.14	0.4848	82.51	27.23	
3.0	0.4021	85.49	26.30	0.5160	81.40	27.06	
3.5	0.4350	84.13	26.28	0.5472	79.84	26.74	
4.0	0.4642	83.18	26.17	0.5773	78.56	26.46	
4.5	0.4940	81.69	26.14	0.6027	77.24	26.34	

injects excessively large values into the calculated bypass, causing the normalization layers in the denoiser network to behave improperly, and finally introduces these unpleasant artifacts. Furthermore, removing the approximation of $\frac{\partial}{\partial x_{t_i}} \hat{v}_\theta$ introduces unrealistic structural details, such as distorted stones in the first row, deformed bicycles in the second row, and abnormal house shapes in the third row. These visualizations indicate that the introduced approximations not only produce more realistic details but also effectively suppress artifacts that may arise from exponential explosion.

C. More Experiment Results

C.1. More Qualitative Comparison with SOTA Editing Methods

Additional qualitative comparisons are provided in Fig. 10. The results demonstrate that FlowBypass, across different backbones, outperforms other editing methods in terms of both fidelity and alignment.

C.2. User Study

A user study is conducted to provide comprehensive subjective evidence of the visual performance of our method. Participants were asked to compare our results with those produced by state-of-the-art approaches in a pairwise preference setting under controlled viewing conditions. As shown in Fig. 11, our method consistently achieves the highest preference rates across all backbones and comparison methods. In each bar, the green region indicates the proportion of users who preferred our results, while the red region corresponds to the competing method. These results demonstrate that FlowBypass not only improves objective reconstruction fidelity but also delivers outputs that align more closely with human perception.

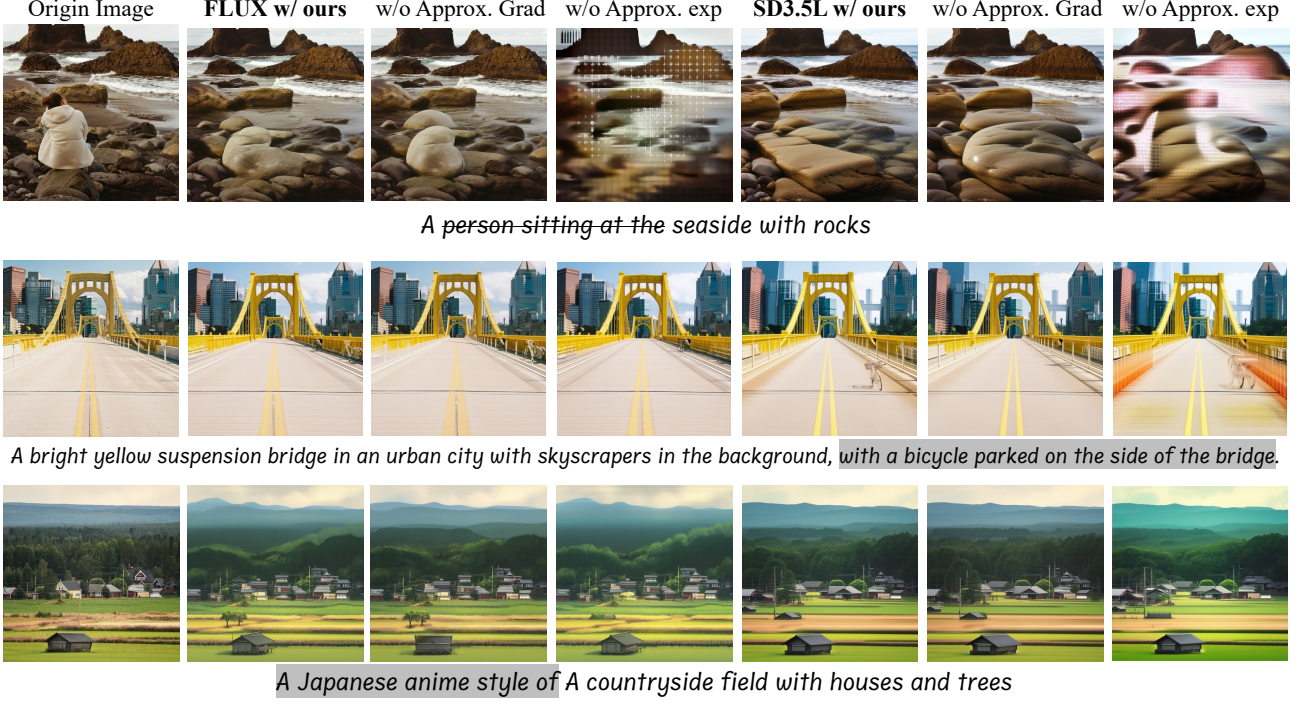


Figure 7. Visual comparison of ablation results on approximation. Zoom in for a better view.

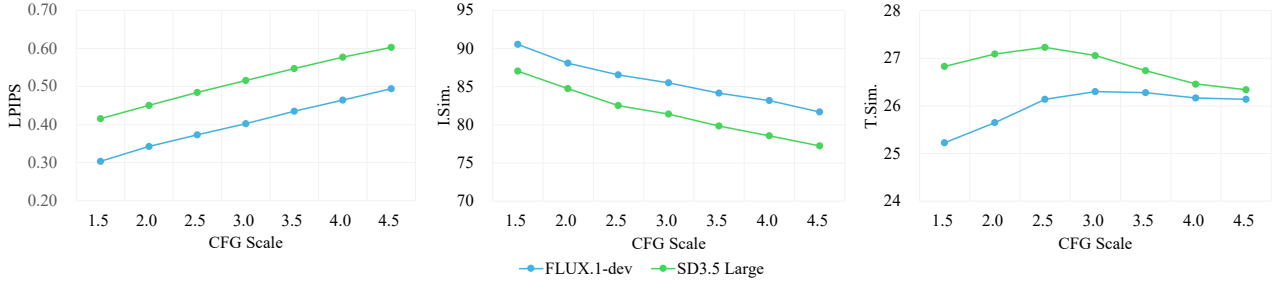


Figure 8. Trends of edit performance as CFG scale ω increases.

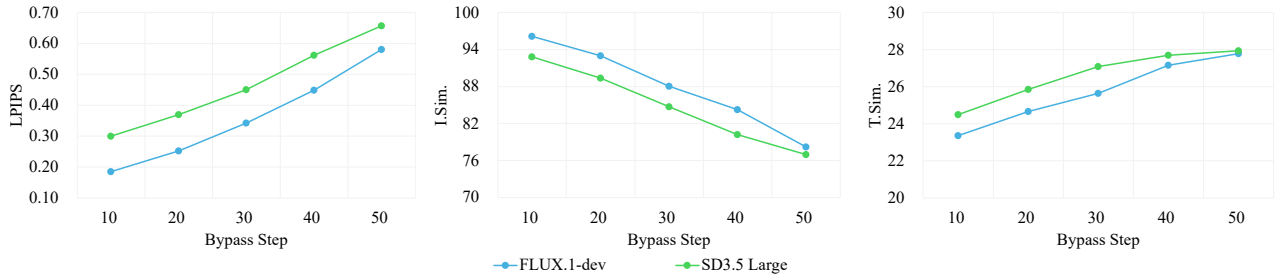
C.3. Runtime Comparison with SOTA Editing Methods

We present a comprehensive runtime comparison against state-of-the-art editing methods in Tab. 7. As specified in Sec. 4.1, all experiments are conducted on a single RTX 4090 GPU. However, FLUX.1-dev cannot be executed naively under the 24GB VRAM limit of the RTX 4090. To ensure functional equivalence while fitting the model into memory, we employ DeepSpeed with ZeRO Stage-3 optimization (Rajbhandari et al., 2020), which preserves computational correctness while reducing memory consumption. It is worth noting that the runtime of FLUX on RTX 4090 is sensitive to system-level factors such as PCIe bandwidth and host RAM capacity. To provide a fairer comparison, we additionally benchmark all methods on a larger-memory GPU (L20) without DeepSpeed, as reported in the fifth column of Tab. 7. Although FlowBypass is not the fastest method in absolute runtime, it achieves a practical processing cost for high-resolution image editing while offering superior performance and a well-balanced between fidelity and alignment.

Additionally, we break down the computational cost into different stages to highlight the extra overhead introduced by the bypass, as shown in Tab. 8. Theoretically, the bypass computation should account for only about 21.1% additional cost, and our practical results confirm this, demonstrating that the bypass is not the primary contributor to the overall computational burden. The discrepancy between the totals reported in Tab. 8 and Tab. 7 comes from the exclusion of text encoding time in Tab. 8.

Table 6. Impact of bypass step.

Backbone	FLUX.1-dev			SD3.5 Large		
	Timestep	LPIPS \downarrow	I.Sim. \uparrow	T.Sim. \uparrow	LPIPS \downarrow	I.Sim. \uparrow
10	0.1849	96.14	23.36	0.3003	92.84	24.50
20	0.2525	92.99	24.66	0.3695	89.37	25.86
30	0.3425	88.06	25.65	0.4507	84.73	27.09
40	0.4490	84.25	27.16	0.5618	80.20	27.70
50	0.5811	78.21	27.78	0.6576	76.95	27.94


 Figure 9. Trends of edit performance as Bypass step t_B changes.

C.4. More Edited Results outside Dataset

To further evaluate the generalization ability of FlowBypass, we conduct image editing experiments on samples outside the EditEvalv2 dataset, as shown in Fig. 12. The origin images are selected from four sources, namely the impressionist painting of Claude Monet (first of row 2), the natural image dataset Flickr2K (Timofte & Agustsson, 2017), the image generated by SD3.5L (second of row 4), and Pexels online website¹ (second and third of row 6). The results indicate that FlowBypass can effectively edit diverse types of images with fidelity and alignment, which demonstrates its general editing capability. We also observe that the fidelity is slightly lower when editing the SD3.5L-generated image compared with natural images, as shown in the last of fourth row. This difference may be caused by the domain gap of generation characteristics between FLUX and SD3.5L. In general, FlowBypass can still handle images that follow the unseen distribution during training to provide outputs with desired editing and fidelity to the original image.

C.5. Impact of CFG Scale

We conduct ablation experiments on the CFG scale ω to examine the effect of different guidance strengths on editing performance, with results presented in Fig. 8. As the CFG scale increases, fidelity gradually decreases, while alignment first improves and then declines. When the CFG scale becomes excessively large, overly strong guidance introduces noticeable artifacts and abnormal appearances. Fig. 13 illustrates this trend, showing that smaller CFG scales preserve fidelity but limit alignment, whereas larger CFG scales behave more aggressively and may even introduce severe artifacts. Based on these findings, we set the CFG scale ω to 2 in our experiments. The detailed statistical results are provided in Tab. 5.

C.6. Impact of Hyperparameter ζ

We perform ablation study on the hyperparameter ζ in Equ. 12. The results in Tab. 9 indicate that FlowBypass is reasonably robust to ζ , and varying it within a practical range does not meaningfully influence editing quality, which partially validates the assumption underlying the Taylor expansion in Equ. 12.

¹[Online] Available at <https://www.pexels.com>

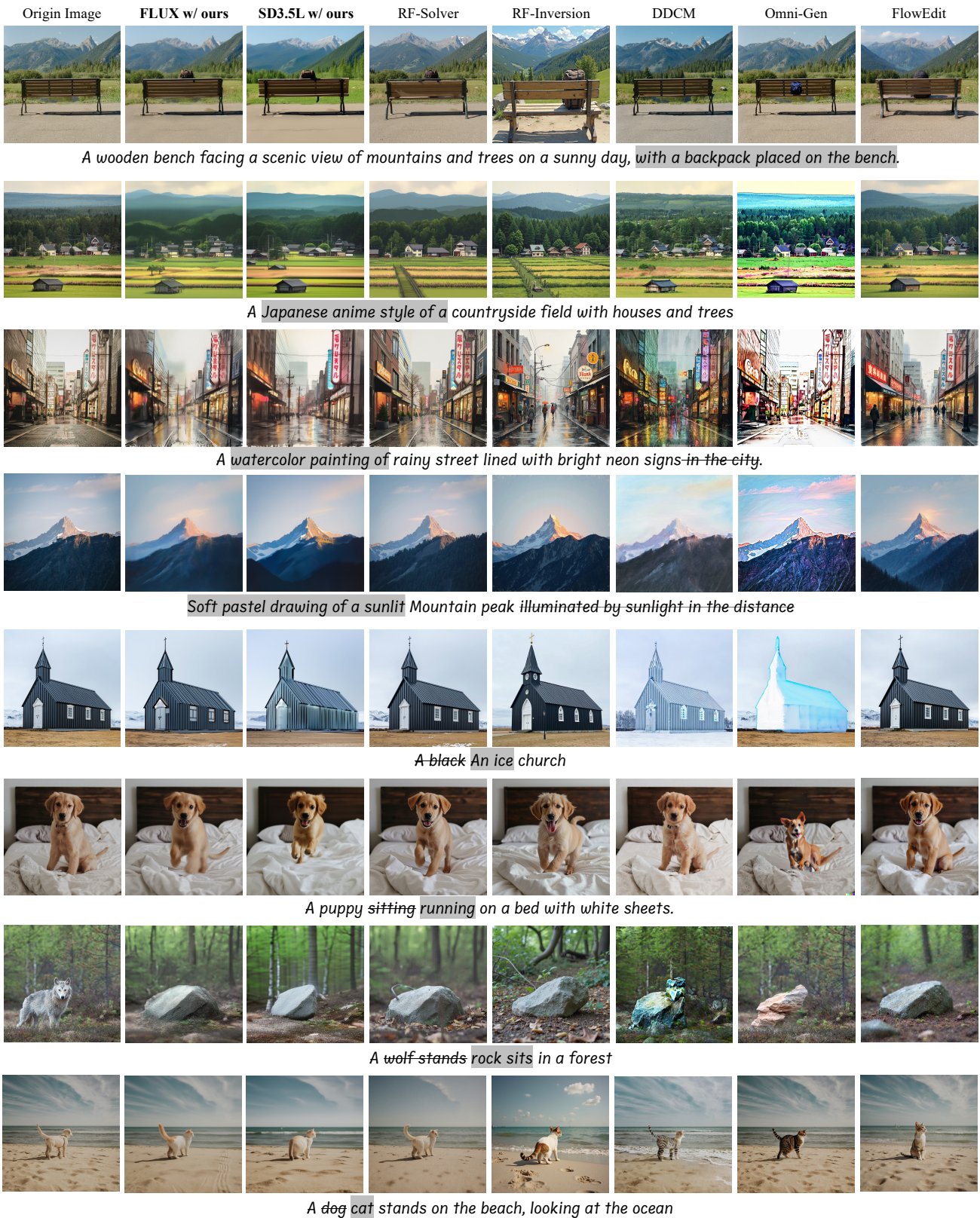


Figure 10. More qualitative comparison with SOTA editing methods. Zoom in for a better view.

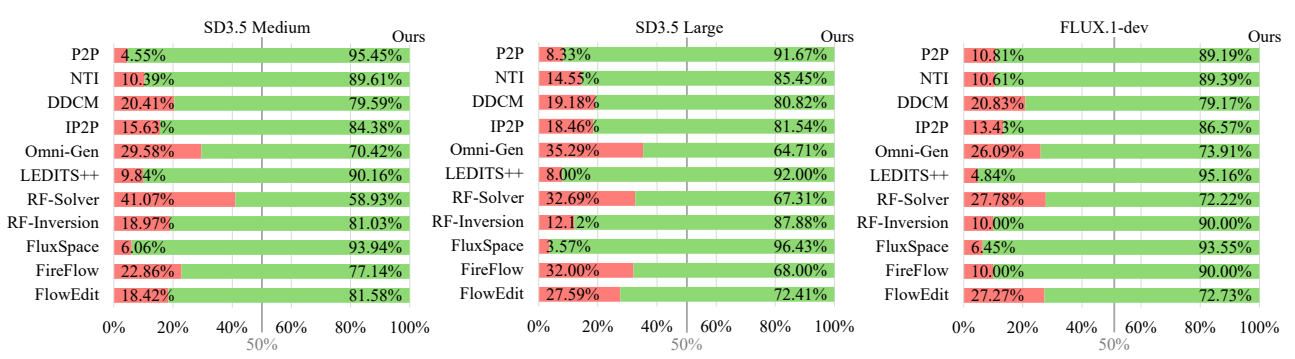


Figure 11. User Study Statistics. The green portion represents the percentage of users who rated our method’s output as better, while the red portion represents the percentage who preferred the output of the compared method.

Table 7. Runtime comparison with SOTA editing methods at 1024×1024 resolution. The # in parentheses indicates the ranking.

Method	Backbone	Precision	4090 Runtime (s) \downarrow	L20 Runtime (s) \downarrow
P2P*	SD1.4	FP32	17.59 (#3)	24.41 (#4)
NTI	SD1.4	FP32	424.03 (#14)	651.65 (#14)
DDCM	LCM v7	FP16	5.36 (#1)	6.47 (#1)
IP2P	SD1.4	FP32	8.28 (#2)	22.16 (#3)
Omni-Gen	Phi-3	FP32	81.59 (#8)	101.84 (#11)
LEDITS++	SD 1.5	FP32	33.19 (#6)	45.18 (#7)
RF-Solver	FLUX.1-dev	BF16	256.23 (#13)	138.33 (#12)
RF-Inversion	FLUX.1-dev	BF16	117.24 (#10)	51.78 (#8)
FluxSpace*	FLUX.1-dev	BF16	145.50 (#11)	65.75 (#9)
FireFlow	FLUX.1-dev	BF16	29.85 (#5)	20.66 (#2)
FlowEdit	FLUX.1-dev	BF16	101.08 (#9)	43.95 (#6)
FlowBypass	SD3.5 Medium	FP16	29.43 (#4)	35.90 (#5)
FlowBypass	SD3.5 Large	FP16	64.11 (#7)	81.31 (#10)
FlowBypass	FLUX.1-dev	BF16	172.24 (#12)	192.23 (#13)

C.7. Impact of Bypass Step

We conduct an ablation study about the impact of bypass step t_B , whose trends are presented in Fig. 9. The results reveal a clear trade-off between fidelity and alignment, where fidelity decreases monotonically and alignment increases monotonically as t_B increases, as demonstrated in Fig. 14. We choose $t_B = 30$ for the best balance between fidelity and alignment. The detailed statistical results are provided in Tab. 6.

C.8. Ablation Study on Different Reconstruction Timestep without Bypass

We conduct an ablation study to evaluate the performance of the inversion–reconstruction editing paradigm when no bypass is introduced, and the reconstruction starts not from pure noise but from an intermediate latent state. As shown in Tab. 10, when starting from larger t , fidelity is difficult to maintain, whereas starting from smaller t compromises alignment. This observation is further supported by the visual examples in Fig. 15, where direct reconstruction from $t = 30$ yields under-edited outputs, whereas reconstruction from $t = 50$ introduces spurious changes, such as altering the dog’s appearance. This phenomenon provides evidence from opposite that FlowBypass addresses the trade-off by correctly jumping the reconstruction starting point onto the reconstruction trajectory, achieving a balance between fidelity and alignment and yielding more stable, high-quality edits.

C.9. Visualization of Bypass b_t under Different t

We present a series of visualizations of bypass b_t under different t during editing. We would like to clarify that FlowBypass performs only one bypass computation and transition during an actual editing process. This visualization is performed solely

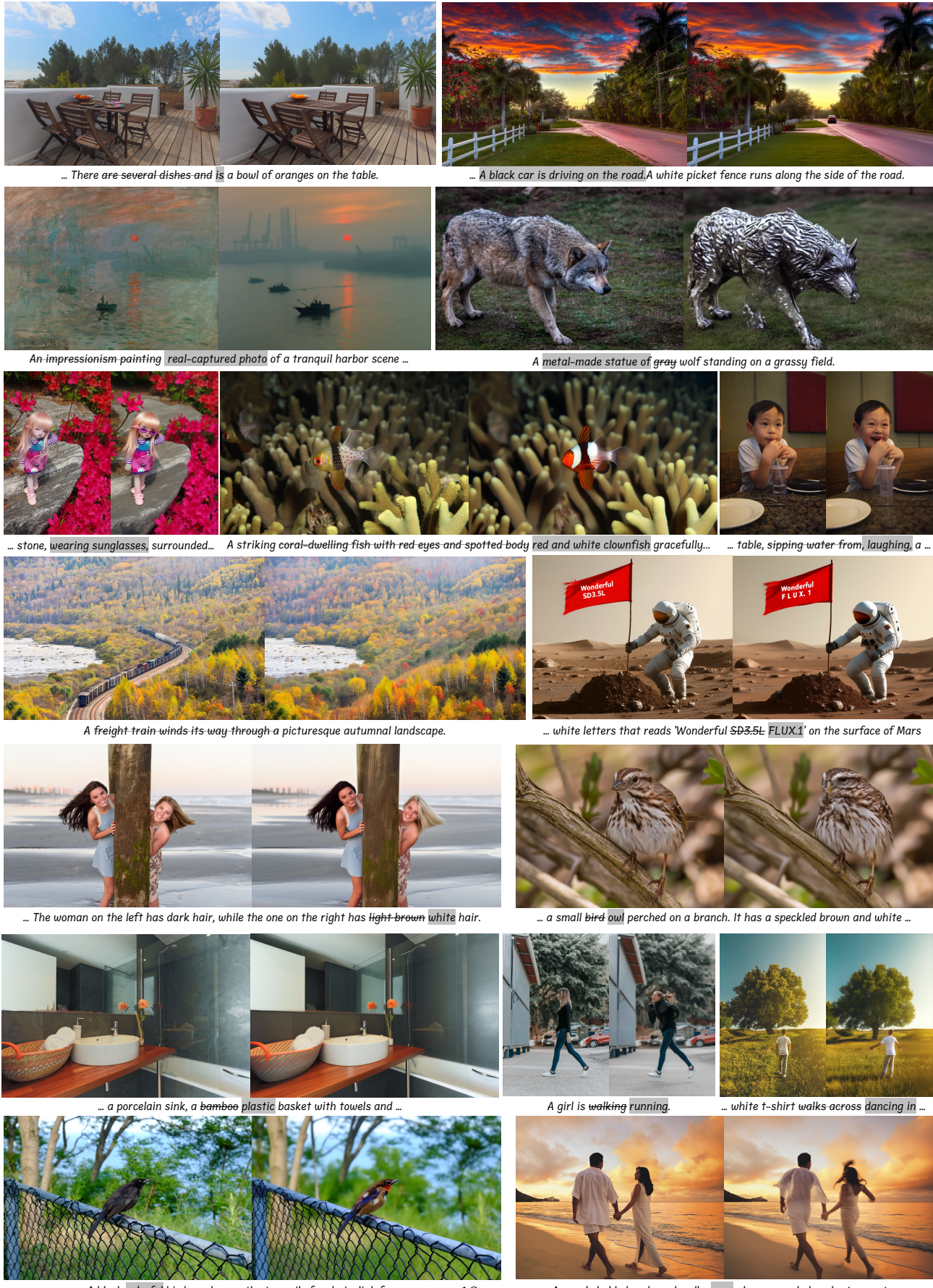


Figure 12. Edit results outside the dataset. Zoom in for a better view.

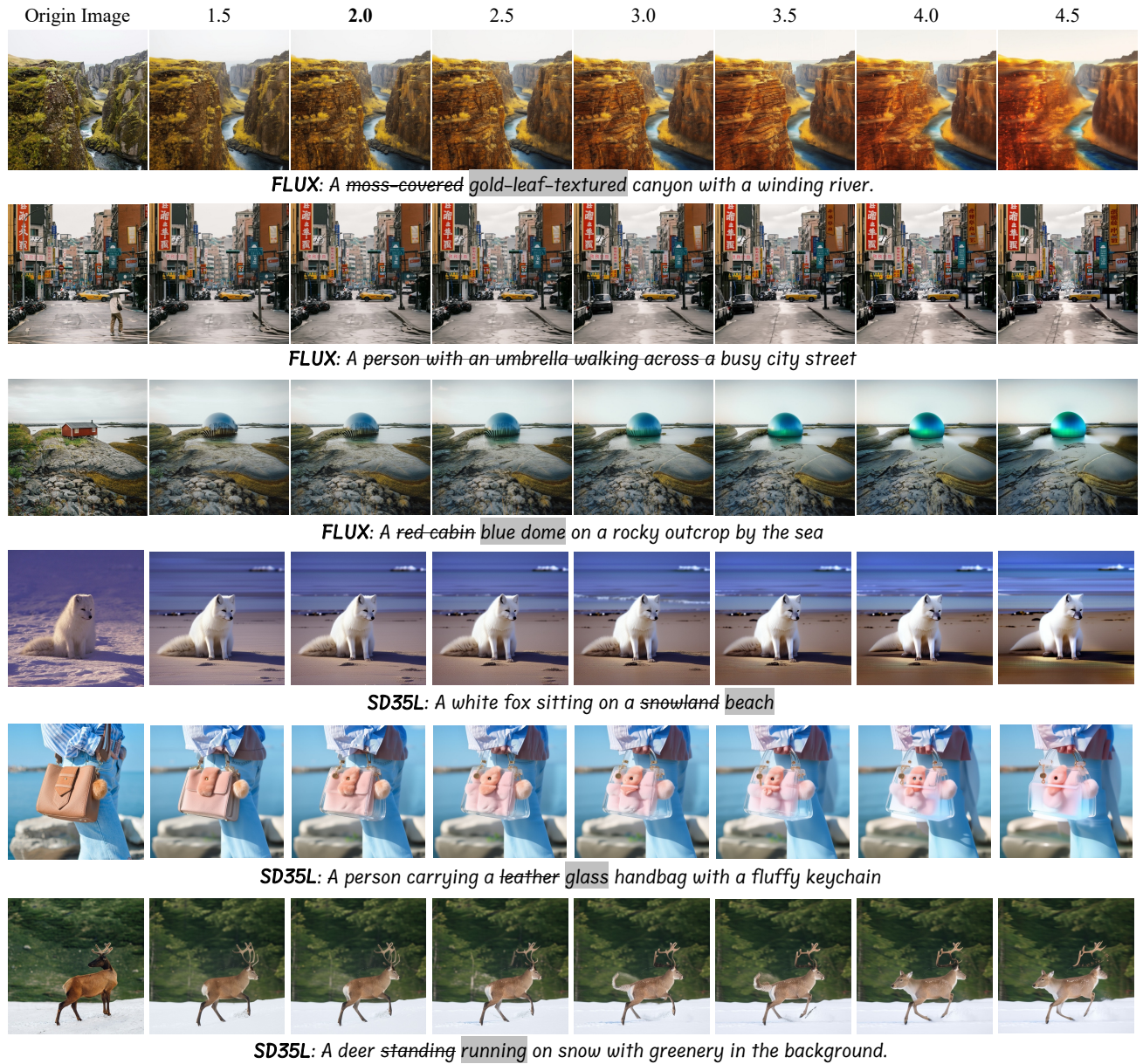


Figure 13. Visual comparison of ablation results on different CFG scales. Zoom in for a better view.

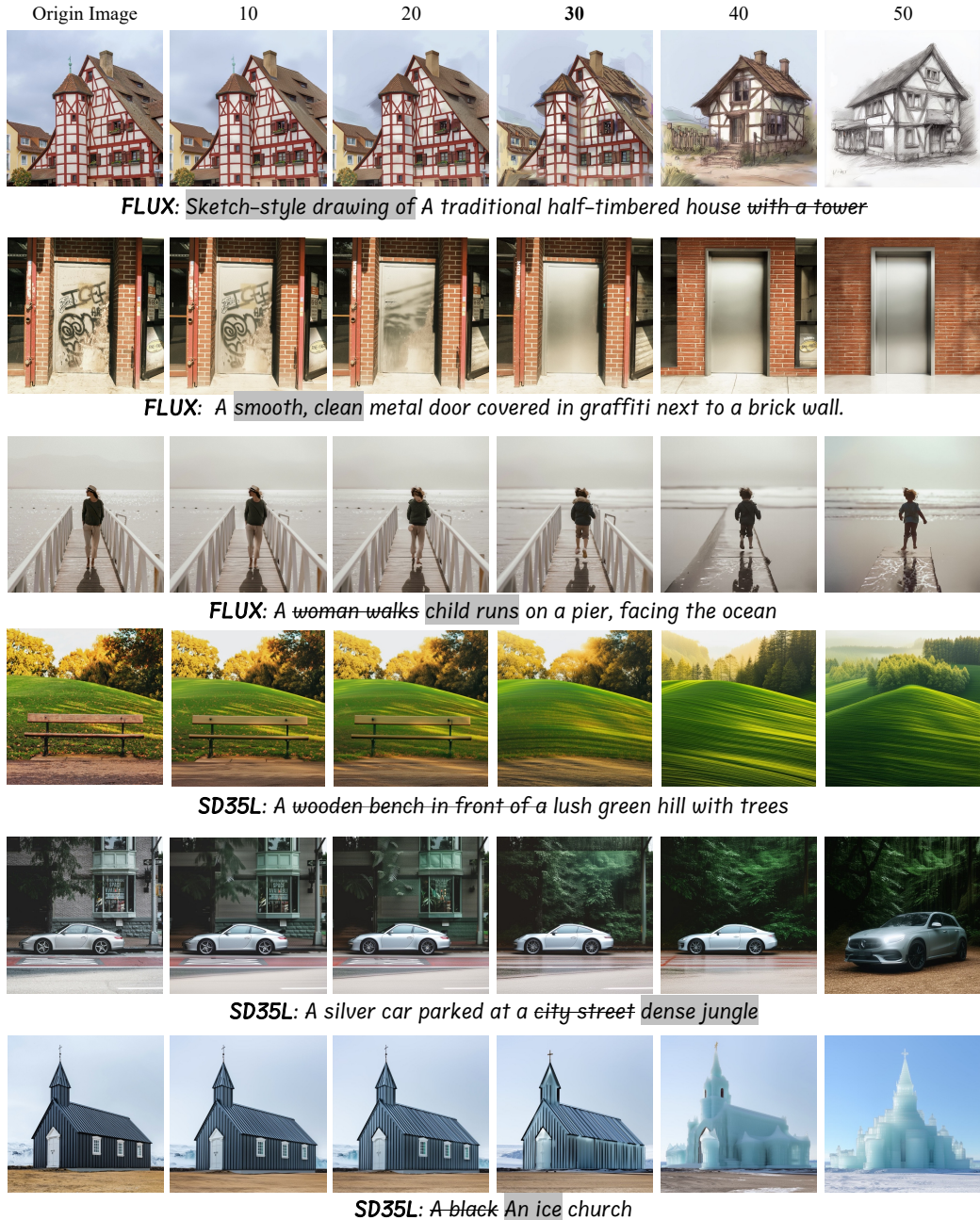


Figure 14. Visual comparison of ablation results on different bypass steps. Zoom in for a better view.

Table 8. Computational cost breakdown (second). The % in parentheses indicates the percentage.

Stage	SD35M	SD35L	FLUX.1
Inversion for Bypass	0.23 (1.08%)	0.16 (0.31%)	0.22 (0.13%)
	9.71 (46.25%)	24.38 (46.97%)	78.50 (46.52%)
	4.32 (20.56%)	10.84 (20.87%)	34.89 (20.67%)
	0.00836 (0.0398%)	0.00335 (0.006461%)	0.00359 (0.002129%)
	6.42 (30.56%)	16.27 (31.34%)	54.90 (32.53%)
	0.32 (1.51%)	0.26 (0.50%)	0.24 (0.14%)

 Table 9. Impact of hyperparameter ζ .

Backbone	FLUX.1-dev			SD3.5 Large		
	ζ	LPIPS \downarrow	I.Sim. \uparrow	T.Sim. \uparrow	LPIPS \downarrow	I.Sim. \uparrow
0.001	0.3290	88.56	25.66	0.4513	84.77	27.10
0.005	0.3446	87.91	25.77	0.4488	85.09	27.14
0.01	0.3425	88.06	25.65	0.4507	84.73	27.09
0.05	0.3509	88.03	25.84	0.4606	84.65	27.21
0.1	0.3434	88.25	25.82	0.4562	84.81	27.32

to illustrate how the bypass behaves when applied at different bypass timesteps. As illustrated in Fig. 16, larger values of t_B (*i.e.*, earlier denoising stages) tend to influence global layout and structure, while smaller values of t_B (*i.e.*, later denoising stages) exhibit the modification of local details and texture refinement. This pattern aligns well with observations reported in prior works on DDIM and RF-based sampling, and provides an intuitive view of how the bypass mechanism modulates semantic corrections across the trajectories.

D. Limitation

Despite its effectiveness, FlowBypass still presents several limitations that highlight opportunities for future improvement. First, FlowBypass do not show its superiority on editing speed, as computing the bypass term b_t imposes additional overhead. Although FlowBypass is not the fastest method in absolute runtime, it achieves a practical processing cost for high-resolution image editing while offering superior performance and a well-balanced between fidelity and alignment. Second, FlowBypass shows limited reliability on negation-based prompts (*e.g.*, “without”). Such edits may fail because the backbone generative backbones inherently struggle with negative conditioning. For instance, prompts such as “a cat without a hat” often still produce a cat wearing a hat. This issue is shared by many editing methods built upon these backbones, as the models themselves provide weak and unreliable outputs for negation. Reformulating negation into affirmative phrasing (*e.g.*, “a cat with a hat” \rightarrow “a cat”) yields more stable and reasonable results.

Table 10. Ablation study on different reconstruction timesteps without bypass.

Backbone	FLUX.1-dev			SD3.5 Large		
	Rec. t	LPIPS↓	I.Sim.↑	T.Sim.↑	LPIPS↓	I.Sim.↑
10	0.1585	97.56	22.35	0.2561	95.50	22.81
20	0.1834	96.94	22.88	0.2817	94.31	23.82
30	0.2240	94.47	23.85	0.3288	91.01	25.36
40	0.3358	88.32	25.53	0.4487	84.43	26.72
50	0.5811	78.21	27.78	0.6576	76.95	27.94
30 w/ Bypass	0.3425	88.06	25.65	0.4507	84.73	27.09

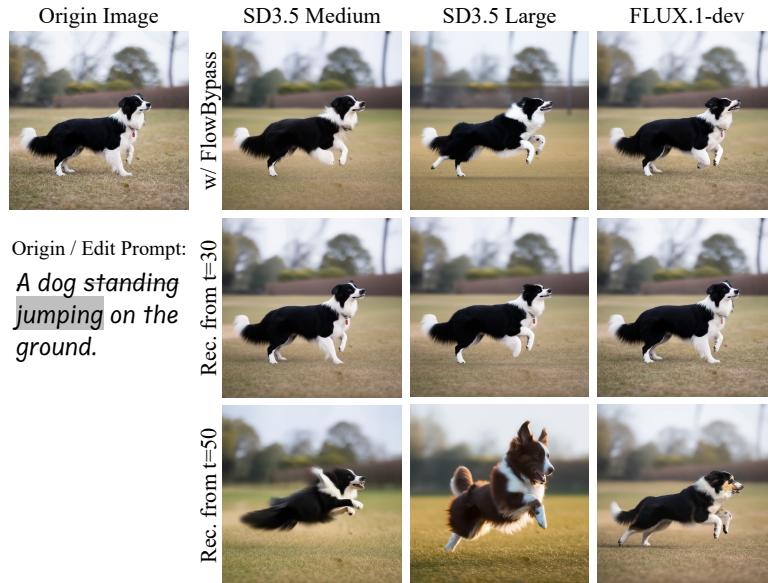


Figure 15. Example outputs from different backbones and different reconstruction timesteps. Zoom in for a better view.



Figure 16. **Visualization of bypass under different t_B .** Zoom in for a better view.